

Design of Robust Raman Pulses for Cold Atom Interferometers Based on the Krotov Algorithm

Ziwen Song*

Independent Researcher, Yungang District, Datong, Shanxi 037000, China

(Dated: February 17, 2026)

The performance of high-precision cold-atom interferometers, which are important for applications in gravimetry and fundamental physics, is often limited by noise and imperfections in the driving laser system. To address this, we propose and numerically demonstrate a method for designing robust Raman pulses using the Krotov quantum optimal control algorithm. We establish a theoretical model for the atom-laser interaction and detail the implementation of the Krotov method to optimize the temporal shape of the pulse's amplitude and phase. Numerical simulations indicate that, compared to standard pulses, the optimized pulses maintain high atomic manipulation fidelity over an extended range of laser frequency detunings and intensity fluctuations. Furthermore, in simulations of a full interferometer sequence, this robustness translates to a significant enhancement in the final fringe contrast under a systematic detuning. This work demonstrates that quantum optimal control is a promising pathway for suppressing experimental noise and improving the signal-to-noise ratio and precision of next-generation atomic sensors.

I. INTRODUCTION

Precision gravity measurement is an indispensable core technology in frontier fields such as geodesy[1], geophysical exploration[2], tests of fundamental physics[3, 4], and inertial navigation[5–7]. With the continuous advancement of science and technology, increasingly stringent requirements are being placed on the precision of measuring the gravitational field and its dynamic variations. Among the numerous measurement techniques, quantum gravimeters based on the principle of cold-atom interferometry utilize the coherent interaction between lasers and atomic wave packets to precisely map inertial information, such as gravitational acceleration, onto the quantum phase of the atoms[8]. Owing to their extremely high theoretical sensitivity, long-term stability, and measurement accuracy, they have become one of the most promising technical approaches in this domain, demonstrating significant advantages in areas such as determining the fundamental gravitational constant[9, 10] and testing the equivalence principle[11, 12].

A typical Mach-Zehnder (MZ) atom interferometer employs a sequence of laser pulses—commonly a $\pi/2$ - π - $\pi/2$ sequence of Raman pulses—to coherently manipulate the atomic wave packet through splitting, reflection, and recombination. Under ideal conditions, the output atomic population exhibits a clear sinusoidal relationship with the phase difference accumulated along the interferometric paths, resulting in a fringe contrast approaching 100%. However, in a realistic experimental environment, noise and imperfections in the laser system are key bottlenecks that limit the interferometer's actual performance[13]. Laser frequency drifts, intensity fluctuations, and errors in pulse duration all prevent the Raman pulses from precisely controlling the

atomic states, thereby reducing the pulse fidelity. Such control errors directly degrade the coherence of the interferometric process, leading to a significant reduction in the final fringe contrast and severely affecting the signal-to-noise ratio and ultimate precision of the gravity measurement[14, 15]. Therefore, designing laser pulses that are robust against experimental noise while maintaining high fidelity is a central challenge for further enhancing the performance of atom interferometers.

To address this challenge, pulse-shaping techniques originating from the field of nuclear magnetic resonance (NMR), along with quantum optimal control theory, provide powerful tools for designing highly robust atomic manipulation schemes[16–18]. The core idea is that by precisely modulating the amplitude and phase of the laser pulses over time, the quantum state can be guided to actively compensate for undesired phases introduced by external noise during its evolution, thereby reaching the target state with extremely high fidelity even in the presence of errors.

Building on the ideas discussed above, this paper aims to apply the Krotov quantum optimal control algorithm to the design of crucial Raman mirror pulses in cold-atom interferometers. The Krotov algorithm is widely used in the field of quantum control due to its high iterative efficiency and monotonic convergence[19–21]. We will first establish a theoretical model for the interaction between a two-level atomic system and the laser field in the interferometer. Subsequently, we will detail the optimization procedure of the Krotov algorithm and its specific implementation in this study. Finally, through extensive numerical simulations, we will systematically evaluate the fidelity and robustness of the optimized pulses and compare their performance with that of conventional pulses under typical errors, such as laser detuning and intensity fluctuations. By simulating the resulting interference fringes, we will verify the significant improvement in fringe contrast achieved by the optimized pulses, thereby demonstrating the feasibility and superiority of

* szw15235225125@gmail.com

this method for enhancing the precision of gravity measurements.

II. THEORETICAL FRAMEWORK

A. Quantum State Evolution

In gravimetry, atom interferometers are typically based on two-photon stimulated Raman transitions. We consider an alkali rubidium atom undergoing stimulated transitions between its hyperfine split energy levels. A stimulated Raman transition can be described as a two-photon process where two atomic states are coupled by two laser fields of different frequencies via an intermediate level. This process can be effectively approximated as a two-level system, as depicted in the energy level diagram in Fig. 1. We denote the ground state by $|g, \mathbf{p}\rangle$ (corresponding to $5^2S_{1/2}, F = 1$) and the excited state by $|e, \mathbf{p} + \hbar\mathbf{k}_L\rangle$ (corresponding to $5^2S_{1/2}, F = 2$). Using the Bloch sphere representation, this quantum state can be written as[22]:

$$|\psi\rangle = \cos\left(\frac{v}{2}\right)|g\rangle + e^{i\phi}\sin\left(\frac{v}{2}\right)|e\rangle, \quad (1)$$

where v and ϕ are the polar and azimuthal angles on the Bloch sphere, respectively.

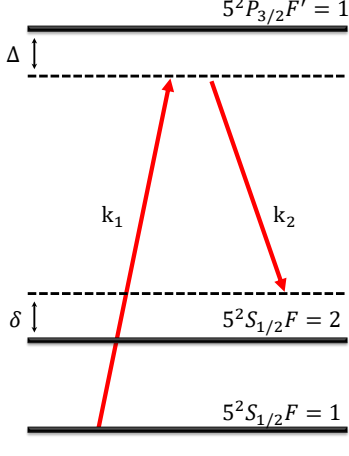


FIG. 1. Energy level diagram for a two-photon stimulated Raman transition in an alkali atom (rubidium as an example). Two laser fields (with wave vectors \mathbf{k}_1 and \mathbf{k}_2) coherently couple the ground-state hyperfine levels. δ is the two-photon detuning, which corresponds to the detuning term in the effective two-level model.

The Hamiltonian for this two-level atomic system interacting with the laser field is given by $H = \frac{\hbar}{2}\Omega_R(t)\cdot\sigma$, which can be expressed in matrix form as:

$$H = \frac{\hbar}{2} \begin{pmatrix} \delta & \Omega_{\text{eff}}e^{-i\phi_L} \\ \Omega_{\text{eff}}e^{i\phi_L} & -\delta \end{pmatrix}. \quad (2)$$

The Schrödinger equation can then be expressed as:

$$\begin{aligned} \frac{d}{dt} \begin{pmatrix} c_e(t) \\ c_g(t) \end{pmatrix} &= -i\frac{\hbar}{2}\Omega_R(t)\cdot\sigma \begin{pmatrix} c_e(t) \\ c_g(t) \end{pmatrix} \\ &= -iH \begin{pmatrix} c_e(t) \\ c_g(t) \end{pmatrix}. \end{aligned} \quad (3)$$

where σ represents the Pauli matrices and $\Omega_R(t)$ is the Rabi vector, given by $\Omega_R(t) = \Omega_{\text{eff}}(t)\cos(\phi_L)\mathbf{x} + \Omega_{\text{eff}}(t)\sin(\phi_L)\mathbf{y} + \delta(t)\mathbf{z}$. Here, $\Omega_{\text{eff}}(t)$ is the effective Rabi frequency and ϕ_L is the phase of the Raman laser. The magnitude of the Rabi vector, $\Omega(t) = \sqrt{\Omega_{\text{eff}}(t)^2 + \delta(t)^2}$, also depends on the two-photon detuning $\delta(t)$, which is given by[23]:

$$\begin{aligned} \delta(t) &= (\omega_1(t) - \omega_2(t)) \\ &- \left(\omega_{eg} + \frac{\mathbf{p}\cdot\mathbf{k}_{\text{eff}}}{m} + \frac{\hbar|\mathbf{k}_{\text{eff}}|^2}{2m} + \delta^{ac} \right). \end{aligned} \quad (4)$$

In this expression, $\mathbf{p}\cdot\mathbf{k}_{\text{eff}}/m = \mathbf{k}_{\text{eff}}\cdot\mathbf{v}$ is the Doppler shift, which contains information about the gravitational acceleration experienced by the atom cloud; $\hbar|\mathbf{k}_{\text{eff}}|^2/2m$ is the two-photon recoil shift, and δ^{ac} is the AC Stark shift. Figure 2 shows the basic working principle of a Mach-Zehnder atom interferometer. Here, the atomic wave packet (purple solid lines) evolves in the gravitational field (g) and is coherently manipulated by a $\pi/2$ - π - $\pi/2$ Raman pulse sequence (timing diagram below) for splitting, reflection, and recombination, ultimately forming a closed interferometric loop.

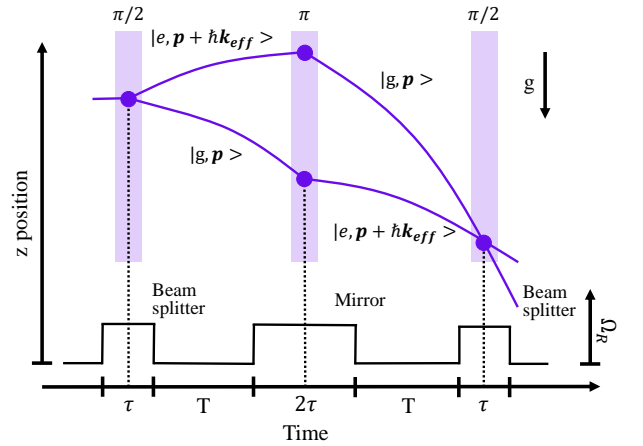


FIG. 2. Spacetime path diagram for a Mach-Zehnder atom interferometer. The interferometer is formed by a $\pi/2$ - π - $\pi/2$ sequence of Raman pulses, with a time interval of T between pulses. The purple solid lines represent the two classical paths of the atomic wave packet under the influence of the gravitational field (g). Here, $|g, \mathbf{p}\rangle$ denotes the ground-state atom and $|e, \mathbf{p} + \hbar\mathbf{k}_L\rangle$ denotes the excited-state atom. The black curve below shows the timing of the Raman pulses, and Ω_R is the Rabi frequency.

While the Schrödinger equation can be solved numerically, the quantum state evolution after applying a Ra-

man pulse of duration Δt can also be described by the propagator[24]:

$$U = e^{-iH\Delta t/\hbar} = \begin{pmatrix} C & -iS \\ -iS^* & C^* \end{pmatrix}, \quad (5)$$

where C and S are defined as[25]:

$$C = \cos \left(\frac{\sqrt{\Omega_{\text{eff}}^2 + \delta^2}}{2} \Delta t \right) + i \frac{\delta}{\sqrt{\Omega_{\text{eff}}^2 + \delta^2}} \sin \left(\frac{\sqrt{\Omega_{\text{eff}}^2 + \delta^2}}{2} \Delta t \right), \quad (6)$$

$$S = e^{i\phi_L} \frac{\Omega_{\text{eff}}}{\sqrt{\Omega_{\text{eff}}^2 + \delta^2}} \sin \left(\frac{\sqrt{\Omega_{\text{eff}}^2 + \delta^2}}{2} \Delta t \right). \quad (7)$$

The transition probability P_e after the application of the Raman pulse can be calculated from $P_e = |\langle e|U|\psi_0 \rangle|^2$ [26]. For an arbitrary pulse shape, the analytical solution is complex. However, by employing the Magnus expansion to obtain a perturbative expansion in Δt , one can calculate an effective propagator for a given pulse's action on the two-level system[27, 28].

$$U = \exp(-i(H_0 + H_1 + H_2 + \dots) \Delta t/\hbar) = U_0 U_1 \dots U_n \dots U_{N-1} U_N. \quad (8)$$

The propagator for each time step is treated as the action of a short rectangular pulse with a fixed laser amplitude and phase, acting on the atoms for a duration dt .

Therefore, the quantum state after evolving under the modulated pulse can be expressed as:

$$|\psi_e \rangle = U|\psi_0 \rangle. \quad (9)$$

B. Atomic Velocity Distribution

In an ideal atom interferometer, the Raman lasers have identical transverse intensity profiles, the laser frequency is stable, and the atomic cloud has a zero-velocity spread. Under these conditions, the maximum fringe contrast is obtained. When the velocity spread of the atom cloud is broader than the Raman transition linewidth, parasitic interferometric paths can emerge. These paths, which arise from atoms imperfectly following the intended trajectory shown in Fig. 1 during the splitting and recombination processes, are a primary cause of reduced fringe contrast. Other contributing factors include imbalanced population splitting due to imperfect beam-splitter pulses and dephasing effects arising from velocity-dependent phase accumulation[21, 29].

In this section, we focus on the impact of the atomic velocity distribution on fringe contrast. In experiments, the Raman laser frequency is typically chirped to compensate for the acceleration of the atomic cloud's center-of-mass along the z -axis due to gravity. However, this chirp does not compensate for the relative motion between atoms

arising from their thermal velocity spread. Therefore, we primarily consider the dephasing effects caused by this thermal motion. For a cold atom cloud undergoing thermal expansion, both the atomic positions and velocities can be modeled by Gaussian distributions. Assuming the position and velocity distributions are independent, the initial probability distribution for an atom with phase-space coordinates $(x_0, y_0, z_0, v_{x0}, v_{y0}, v_{z0})$ is given by[30]:

$$\mathcal{N}(x_0, y_0, z_0, v_{x0}, v_{y0}, v_{z0}) = \prod_{i \in \{x, y, z\}} g(i_0, \sigma_i) g(v_{i0}, \sigma_v). \quad (10)$$

Here, $g(x, \sigma) = (2\pi\sigma^2)^{-1/2} \exp(-x^2/(2\sigma^2))$ is the general expression for a normalized one-dimensional Gaussian distribution, where x corresponds to an initial position i_0 or velocity v_{i0} .

The temperature of the atom cloud affects the initial velocity distribution, leading to a velocity-dependent detuning $\delta(t)$. To account for this, one must integrate over the entire thermal velocity range to obtain the total transition probability[23, 26, 29]:

$$P_e = \int |c_e(\mathbf{v})|^2 g(\mathbf{v}) d^3 \mathbf{v}, \quad (11)$$

where $c_e(\mathbf{v})$ is the final probability amplitude of the excited state for an atom with initial velocity \mathbf{v} , and $g(\mathbf{v})$ is the initial atomic velocity distribution.

C. Fringe Contrast

In a three-pulse Mach-Zehnder interferometer sequence, inertial effects such as gravitational acceleration induce a relative phase shift between the two paths of the interferometer. A final $\pi/2$ pulse converts this phase difference into a population difference between the final atomic states. For a counter-propagating beam configuration and in the limit of small detuning, the total transition probability is given by[26, 31, 32]:

$$P_e = |S_1|^2 |S_2|^2 |S_3|^2 + |C_1|^2 |S_2|^2 |C_3|^2 + |S_1|^2 |C_2|^2 |C_3|^2 + |C_1|^2 |C_2|^2 |S_3|^2 - 2\text{Re} [e^{i\Phi_g} C_1 S_1^* (S_2^*)^2 C_3^* S_3], \quad (12)$$

where C and S are defined as above, and Φ_g is the relative phase induced in the interferometer. This expression can be simplified to the general form:

$$P_e = \frac{1}{2} (A - B \cos(\Phi_g + \phi(\delta))). \quad (13)$$

Here, A represents the interferometer offset, and $\phi(\delta)$ is the relative phase shift introduced by the Raman pulses, given by $\phi S_{\pi/2}^1 + \phi S_{\pi/2}^3 - 2\phi S_\pi$. When the detuning δ is zero and no other phase noise is introduced, the expression simplifies to:

$$P_e = \frac{1}{2} (A - B \cos(\alpha T^2)). \quad (14)$$

To calculate the output transition probability of the interferometer, we use the propagator method. The total operator for the Mach-Zehnder interferometer sequence can be written as:

$$U_{\text{Total}} = U_{\pi/2} U_{T1} U_{\pi} U_{T2} U_{\pi/2}. \quad (15)$$

The total evolution can then be expressed as:

$$|\psi_e\rangle = U_{\text{Total}}|\psi_0\rangle. \quad (16)$$

The final output transition probability is calculated directly from the probability amplitude:

$$P_e = |\langle e | U_{\text{Total}} | \psi_0 \rangle|^2. \quad (17)$$

The final normalized fringe contrast is then given by[26]:

$$C = \frac{\left(\int_v P_e^{d1}(v)g(v)dv\right)_{\max} - \left(\int_v P_e^{d1}(v)g(v)dv\right)_{\min}}{\left(\int_v P_e^{d1}(v)g(v)dv\right)_{\max} + \left(\int_v P_e^{d1}(v)g(v)dv\right)_{\min}}. \quad (18)$$

This formalism, by directly calculating the final state via the time-evolution operator U_{Total} , avoids the reliance on the symmetry of the pulse sequence inherent in traditional methods. Consequently, it provides highly reliable predictions of the transition probability even under conditions involving asymmetric or complex pulses.

D. Pulse-Shaping Techniques

Pulse-shaping techniques were first applied in the field of NMR. The core idea is to modulate the original pulse waveform by replacing the traditionally fixed amplitude and phase with time-varying functions. These functions are then designed using optimization methods to enhance performance metrics such as excitation efficiency, selectivity, and robustness. Amplitude modulation of the pulse alters its response to detuning, while phase modulation affects its sensitivity to errors in Rabi frequency and pulse duration. With modulation, the off-diagonal driving term of the Rabi vector can be expressed in a time-varying form as $\Omega_{\text{eff}}(t)[\cos \phi_L(t)\mathbf{x} + \sin \phi_L(t)\mathbf{y}]$, where $\Omega_{\text{eff}}(t)$ is the amplitude modulation and $\phi_L(t)$ is the phase modulation[33].

Based on the description above, the system Hamiltonian becomes[]:

$$H(t) = \frac{\hbar}{2} (\delta\sigma_z + \Omega_{\text{eff}}(t)[\cos \phi_L(t)\sigma_x + \sin \phi_L(t)\sigma_y]). \quad (19)$$

In the Hamiltonian, δ represents the total detuning of the system, while the second term is determined by the control field, i.e., the instantaneous amplitude $\Omega_{\text{eff}}(t)$ and phase $\phi_L(t)$ of the pulse. Therefore, the physical essence of pulse-shaping techniques is to dynamically manipulate the direction and strength of the effective control field on the Bloch sphere by carefully designing the control functions $\Omega_{\text{eff}}(t)$ and $\phi_L(t)$. This steers the quantum state

vector along a specific trajectory from an initial point to a target point. A robust evolution trajectory should be designed such that its endpoint is insensitive to variations in the uncontrollable components of the field, such as fluctuations in the detuning δ or an overall scaling of the control amplitude $\Omega_{\text{eff}}(t)$.

E. Optimization Method

To achieve high-fidelity and robust control of the Raman mirror pulses in a cold-atom interferometer, we employ the Krotov quantum optimal control algorithm[34, 35]. The core advantage of this algorithm is its monotonic convergence, which enables it to stably and efficiently find the optimal pulse amplitudes and phases required to meet a specific physical objective. The Krotov method aims to minimize a composite cost functional, J , through an iterative procedure. For the approximate two-level system in our cold-atom interferometer, we define this functional J as being composed of three parts[19]:

$$J = J_t + g_a + g_b. \quad (20)$$

The first term is the final-time cost, J_T , which is the primary optimization objective. It quantifies the discrepancy between the final quantum state and the target state, i.e., the infidelity. In our task, the goal is to drive an initial atomic state $|\psi_0\rangle$ to a target state $|\psi_{\text{tgt}}\rangle$ to achieve the high-fidelity population inversion required for a mirror pulse. Therefore, we define J_T as:

$$J_T = 1 - |\langle \psi_{\text{tgt}} | \psi(T) \rangle|^2. \quad (21)$$

Minimizing J_T is equivalent to maximizing the final-state fidelity, which is directly related to the phase measurement precision of the interferometer.

The second term is the running cost on the control field, g_a . This term imposes physical constraints on the control field, i.e., the Raman laser pulse $\epsilon(t)$, to ensure that the optimized pulse waveform is experimentally feasible and reasonable[33, 36]. By penalizing excessively high field strengths or rapid field variations, we can prevent damage to optical equipment, suppress nonlinear effects (such as the AC Stark shift), and simultaneously smooth the temporal waveform and limit its spectral bandwidth[29]. In this study, its specific form is defined as[37]:

$$\begin{aligned} g_a(\epsilon^{(k)}(t)) &= \frac{\lambda}{S(t)} \left(\epsilon^{(k)}(t) - \epsilon^{(k-1)}(t) \right)^2 \\ &= \frac{\lambda}{S(t)} \left(\Delta\epsilon^{(k)}(t) \right)^2. \end{aligned} \quad (22)$$

Here, λ is a step-size parameter, and $\epsilon^{(k-1)}(t)$ is the reference pulse from the previous iteration (or the initial guess). $S(t) \in [0, 1]$ is a shape function that modulates the control field update in the time domain. In this

study, we select a Blackman window as the shape function, which is expressed over the total pulse duration T as:

$$S(t) = 0.42 - 0.5 \cos\left(\frac{2\pi t}{T}\right) + 0.08 \cos\left(\frac{4\pi t}{T}\right), \quad t \in [0, T]. \quad (23)$$

This function satisfies the boundary conditions $S(0) = S(T) = 0$. Consequently, the cost functional imposes an infinite penalty on any non-zero control field at the start and end of the pulse ($t = 0$ and $t = T$). This forces the control field $\epsilon(t)$ generated by the optimization to have zero amplitude at its start and end points, ensuring a smooth turn-on and turn-off.

The third term, g_b , is a state-dependent running cost. This term is associated with the state of the system during its evolution and is used for time-dependent control objectives or to penalize populations in certain subspaces, thereby forcing the evolution path to satisfy physical or technical constraints[38–40]. In open quantum systems, it is often used to suppress decoherence by forcing the system to avoid intermediate states that are particularly susceptible to noise. Since the primary objective of this study is final-state fidelity and we do not consider complex intermediate path constraints in our current model, we set $g_b = 0$.

The Krotov algorithm begins with an initial guess for the control field, $\epsilon^{(0)}(t)$. In the k -th iteration, the updated control field, $\epsilon^{(k)}(t)$, is given by:

$$\epsilon^{(k)}(t) = \epsilon^{(k-1)}(t) + \Delta\epsilon^{(k)}(t). \quad (24)$$

The key to this algorithm is that the construction of its field update term, $\Delta\epsilon^{(k)}(t)$, strictly guarantees the monotonic convergence of the cost functional, i.e., $J^{(k+1)} \leq J^{(k)}$. According to [37, 41], when certain convergence conditions are met, the update equation can be expressed as:

$$\Delta\epsilon^{(k)}(t) = \frac{S(t)}{\lambda} \text{Im} \left[\langle \chi^{(k-1)}(t) | \frac{\partial H}{\partial \epsilon(t)} | \psi^{(k)}(t) \rangle \right]. \quad (25)$$

The calculation of this update requires two auxiliary quantum states, $|\psi^{(k)}(t)\rangle$ and $|\chi^{(k-1)}(t)\rangle$. Here, $|\psi^{(k)}(t)\rangle$ is the quantum state obtained by forward propagation from the initial state $|\psi_0\rangle$ under the new control field $\epsilon^{(k)}(t)$. The state $|\chi^{(k-1)}(t)\rangle$ is the co-state obtained by backward propagation from the final target state $|\psi_{\text{tgt}}\rangle$ under the old control field $\epsilon^{(k-1)}(t)$, incorporating the gradient of the final-time cost J_T .

In designing the control update $\Delta\epsilon^{(k)}(t)$, it is made proportional to the ratio of the update shape function $S(t)$ and the step-size parameter λ :

$$\Delta\epsilon^{(k)}(t) \propto \frac{S(t)}{\lambda}. \quad (26)$$

Theoretically, the monotonic convergence of the Krotov method is only strictly guaranteed in the continuous

limit, where the time step approaches zero. In practical numerical calculations with discrete time steps, the choice of the step-size parameter λ is crucial for the algorithm's performance. This parameter balances the algorithm's convergence speed with its numerical stability. A value of λ that is too small implies a weak penalty on changes in the control field, potentially leading to excessively large update steps that cause numerical instability or even divergence. Conversely, a value of λ that is too large will overly suppress field updates, making the convergence process extremely slow. By applying the Cauchy-Schwarz inequality, a theoretical condition on λ that guarantees convergence can be derived, offering guidance for its selection. In our research, after numerous numerical experiments and careful adjustments, we ultimately chose a value of $\lambda = 0.5$. This value ensures stable convergence of the iterative process while also providing an acceptable rate of convergence. Once determined, this value is kept constant throughout all subsequent optimization calculations.

III. OPTIMIZATION PROCESS AND PULSE PERFORMANCE EVALUATION

A. Optimization Performance (Analysis of Algorithm Convergence)

We use a Gaussian pulse as the initial pulse shape, $\epsilon^{(0)}(t)$, to seed the Krotov algorithm optimization. In Section II, we defined the optimization functional, which includes the running cost on the control field, g_a . The step-size parameter λ therein is a key parameter that directly affects the convergence speed and stability of the algorithm. To investigate its specific impact, we performed optimizations by setting the step-size parameter λ to 0.1, 0.5, and 1.0, respectively. The convergence of the cost functional J as a function of the iteration number for each case is shown in Fig. 3.

As can be clearly observed in Fig. 3, regardless of the value of the step-size parameter λ , the average value of the cost functional J exhibits a monotonically decreasing trend with the number of iterations, eventually converging stably below a threshold of 0.001. This verifies the effectiveness of the Krotov algorithm for this study. After 10 iterations, the average error across the entire ensemble remains relatively high, as errors for certain ensemble members are still significant. Achieving full robustness in just 10 iterations is therefore challenging, but the average error can be reduced below the 0.001 threshold with further iterations. As the optimization approaches the target threshold, a larger number of iterations is required to converge fully. After the average cost functional, $J_T(\text{avg})$, reaches the target threshold, we observe a trade-off: to enhance the pulse's robustness against Hamiltonian fluctuations, the optimization sacrifices some fidelity under unperturbed conditions (represented by $J_T(u = 1)$).

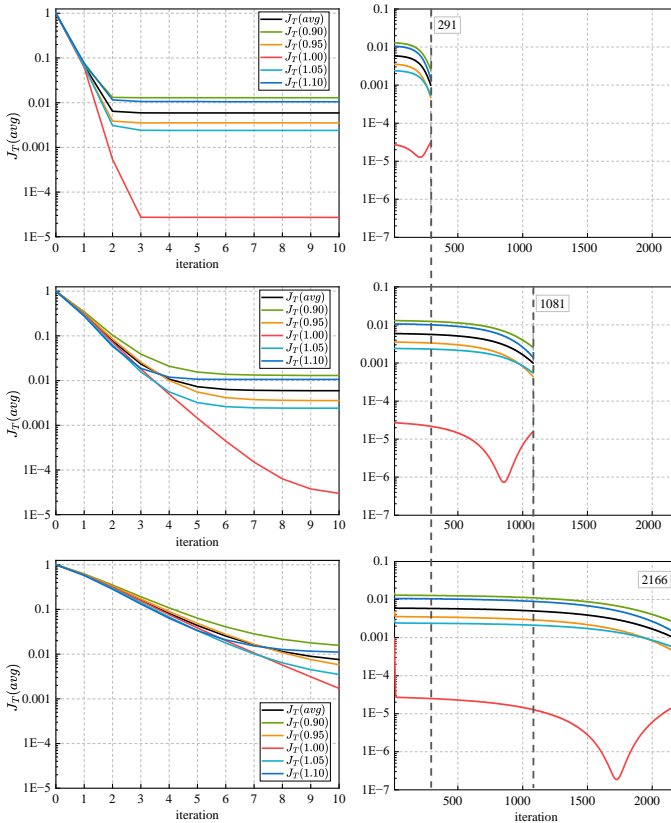


FIG. 3. Convergence process of the Krotov algorithm for different step-size parameters λ . The three rows, from top to bottom, correspond to $\lambda = 0.1, 0.5$, and 1.0 , respectively. The left column shows a magnified view of the first 10 iterations, while the right column shows the complete iterative process. In the plots, the black curves represent the average cost functional, $J_T(\text{avg})$, and the colored curves represent the cost functionals for different perturbation parameters. The results show that $\lambda = 0.5$ achieves the optimal balance between convergence speed and stability.

We can further compare the three convergence curves in Fig. 3 with the time evolution of the normalized amplitude and phase of the resulting mirror pulses after convergence. For $\lambda = 0.1$ (top panel of Fig. 3), the cost functional descends most rapidly in the initial stage. However, while a small λ yields a fast initial convergence, it can lead to excessively large update steps, causing the algorithm to "overshoot" the optimal solution and introduce numerical instability, a tendency visible in the final optimized pulse shape. For $\lambda = 1.0$ (bottom panel of Fig. 3), the convergence process is the most smooth and stable, but also the least efficient, requiring over 2000 iterations to reach a low value of the functional. This indicates that a large λ (implying a strong penalty on control field changes) overly restricts the update amount $\Delta\epsilon(t)$ in each iteration, leading to a slow optimization process. When $\lambda = 0.5$ (middle panel of Fig. 3), this parameter achieves the best balance between convergence

speed and stability. It not only exhibits a rapid convergence capability in the initial stage, similar to the $\lambda = 0.1$ case, but also maintains a smooth and stable downward trend in subsequent iterations, ultimately reaching convergence after approximately 1000 iterations.

A noteworthy phenomenon is that in the initial phase of the optimization, the cost functional for the unperturbed case (red curve) shows a slight increase, while the average cost functional (black curve) and the functionals for other perturbed cases continue to decrease. This is a typical characteristic of robustness optimization: the algorithm trades a portion of the performance under a single, ideal condition for an overall performance enhancement across the entire range of parameter perturbations, thereby achieving stronger robustness.

To provide a more intuitive understanding of how the step-size parameter λ affects the final control field, Fig. 4 displays the time evolution of the normalized amplitude and phase for the final mirror pulses (labeled KR1, KR2, and KR3) obtained from optimizations with $\lambda = 0.1, 0.5$, and 1.0 , respectively. These are compared with the initial, non-robust pulse (black curve). Compared to conventional rectangular or Gaussian pulses, all pulses optimized by the Krotov algorithm (red curves) exhibit highly complex modulated structures. Both their amplitude and phase undergo precise and non-trivial dynamic adjustments throughout the pulse duration. This complex waveform is not random noise, but rather the optimal control strategy "learned" by the algorithm to achieve high-fidelity inversion even in the presence of perturbations. The specific rises, falls, and jumps in the amplitude and phase during the evolution are fundamentally aimed at guiding the quantum state on the Bloch sphere along a specific trajectory that actively cancels out undesired phases introduced by external errors, such as laser detuning.

Furthermore, a noteworthy observation is that the optimized pulse shapes corresponding to $\lambda = 0.5$ (KR2) and $\lambda = 1.0$ (KR3) exhibit a high degree of similarity, whereas the waveform for $\lambda = 0.1$ (KR1) is distinctly different from the other two. This can be explained by the physical meaning of the step-size parameter λ . When the value of λ is large (e.g., 0.5 and 1.0), the optimization algorithm imposes a stronger penalty on modifications to the control field, tending to search for a robust optimal solution in the vicinity of the initial pulse. The similar waveform structures indicate that, for these two parameter values, the algorithm converged to the same optimization "basin," differing only in the optimization intensity. Different initial pulse shapes often lead to the same optimal pulse, which typically exhibits symmetry around its midpoint, a phenomenon also observed in NMR[42, 43]. However, when $\lambda = 0.1$, the minimal penalty grants the algorithm significant freedom, leading to large update steps. The resulting pulse waveform is overly aggressive, introduces additional high-frequency noise, and has poor stability, making it a non-ideal physical solution.

Considering both the convergence performance in

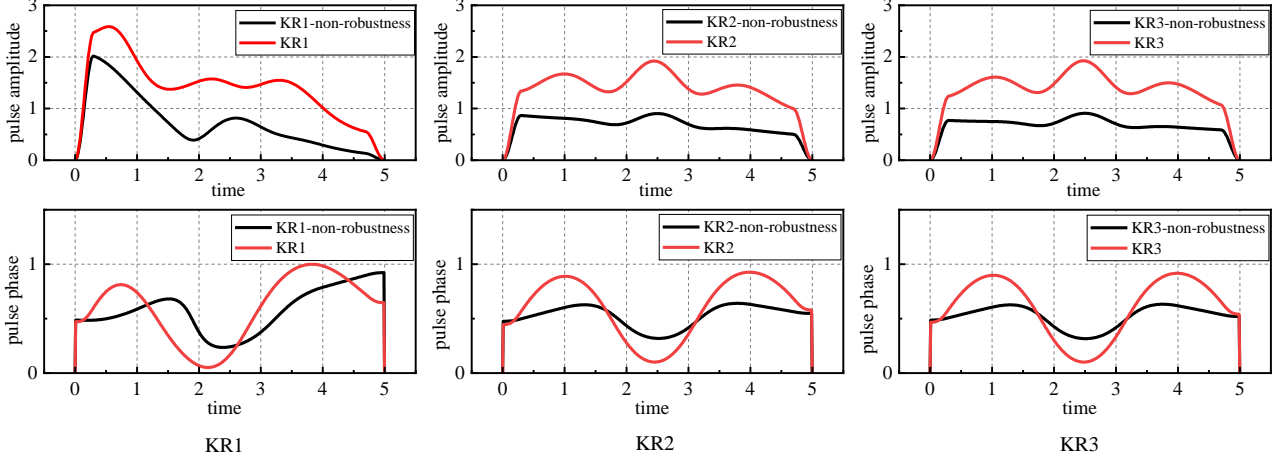


FIG. 4. Final pulse waveforms obtained from optimizations with different step-size parameters λ . The three columns, from left to right, correspond to $\lambda = 0.1$ (KR1), 0.5 (KR2), and 1.0 (KR3), respectively. The top row shows the time evolution of the pulse amplitude, and the bottom row shows the time evolution of the pulse phase. The red curves are the robust pulses optimized by the Krotov algorithm, while the black curves represent the initial non-robust pulse for comparison.

Fig. 3 and the pulse shapes in Fig. 4, we further confirm that $\lambda = 0.5$ is the optimal choice for achieving efficient optimization and generating a high-performance, well-behaved robust pulse. Therefore, the following analysis will focus on the specific performance of the KR2 pulse, which was optimized using this parameter.

B. Pulse Performance

Having verified the effectiveness of the algorithm, this section evaluates the pulse optimized with $\lambda = 0.5$ (hereafter the "Krotov pulse") based on the core metrics of quantum control: fidelity and robustness. Its performance is compared with that of standard amplitude-modulated pulses. In a realistic experimental environment, drifts or inaccuracies in the laser frequency are one of the most common and impactful sources of error. The ability of a pulse to resist such detuning errors is a key indicator of its performance. Figure 5 compares the atomic transition probabilities of the Krotov-optimized pulses (KR1, KR2, KR3) and three standard pulses (rectangular, Gaussian, and super-Gaussian) as a function of laser detuning.

From the comparison in Fig. 5, it can be clearly seen that the response curves of the standard pulses (bottom three panels) show a typical narrow-peak feature for the transition probability as a function of detuning. Their performance is perfect near the zero-detuning point, but the flat-top region is extremely narrow. This means they are extremely sensitive to laser frequency detuning, where even a small frequency shift causes a sharp drop in the transition probability. In contrast, the Krotov-optimized pulses (top three panels) exhibit distinctly superior performance. Their response curves are no longer

single, sharp peaks; instead, they form a broad, multi-peaked plateau structure around the center (zero detuning). This feature implies that even if the laser frequency fluctuates over a considerable range, the Krotov pulses can still maintain an atomic inversion efficiency close to 100%. This "top-hat" type of response curve is a hallmark of highly robust pulses and is crucial for improving the stability and repeatability of atom interferometers. Therefore, the performance evaluation in Fig. 5 provides strong evidence that the pulses designed via the Krotov algorithm are far superior to conventional pulses in terms of robustness against the key error source of laser frequency detuning.

Besides frequency detuning, fluctuations in laser intensity (i.e., variations in the Rabi frequency/coupling strength) are another key source of error. A high-performance pulse should be robust against both types of errors simultaneously. To conduct a more comprehensive evaluation, we have plotted 2D heat maps of the atomic transition probability in a two-parameter error space of detuning and coupling strength, as shown in Fig. 6. In the plots, the horizontal axis represents the normalized coupling strength (with 1.0 being the ideal value), and the vertical axis represents the detuning.

In these heat maps, the color indicates the transition probability (with bright yellow/red areas representing high probability). We can define the region where the transition probability is above a certain threshold (e.g., 0.80) as the "high-fidelity robustness area." The area and shape of this region intuitively reflect the pulse's overall ability to resist composite errors. By comparing the images in Fig. 6, a clear conclusion can be drawn. For the rectangular, Gaussian, and super-Gaussian pulses, the high-fidelity robustness area shows a typical "bull's-eye" or elliptical shape, tightly clustered around the error-

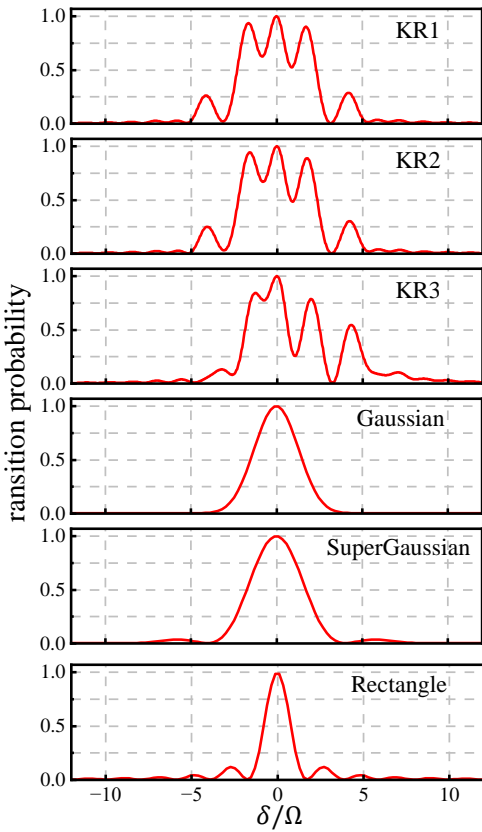


FIG. 5. Comparison of the robustness of different pulses against laser frequency detuning. In the plots, the horizontal axis is the normalized detuning, and the vertical axis is the atomic transition probability. The top three rows show the Krotov-optimized pulses (KR1, KR2, KR3), while the bottom three rows show the standard pulses (Gaussian, super-Gaussian, and rectangular).

free central point (detuning=0, coupling strength=1). As soon as the error parameters deviate from this center, the transition probability drops rapidly. This indicates that their robustness is very limited, effective only within a small range of errors. In contrast, the optimized pulses exhibit a completely different topology. Their high-fidelity robustness areas are no longer simple, centrally symmetric shapes but instead form a large and irregularly shaped "robustness island." The coverage of this area far exceeds that of any standard pulse. This result proves that our optimized pulses can not only resist singular detuning errors but can also maintain excellent and robust performance under more realistic and complex experimental conditions where both laser frequency and intensity fluctuate simultaneously.

To intuitively understand the underlying physical mechanism for the significantly enhanced robustness, we simulated the evolution trajectories of the quantum state on the Bloch sphere under the driving of a standard rectangular pulse and our optimized KR2 pulse in the pres-

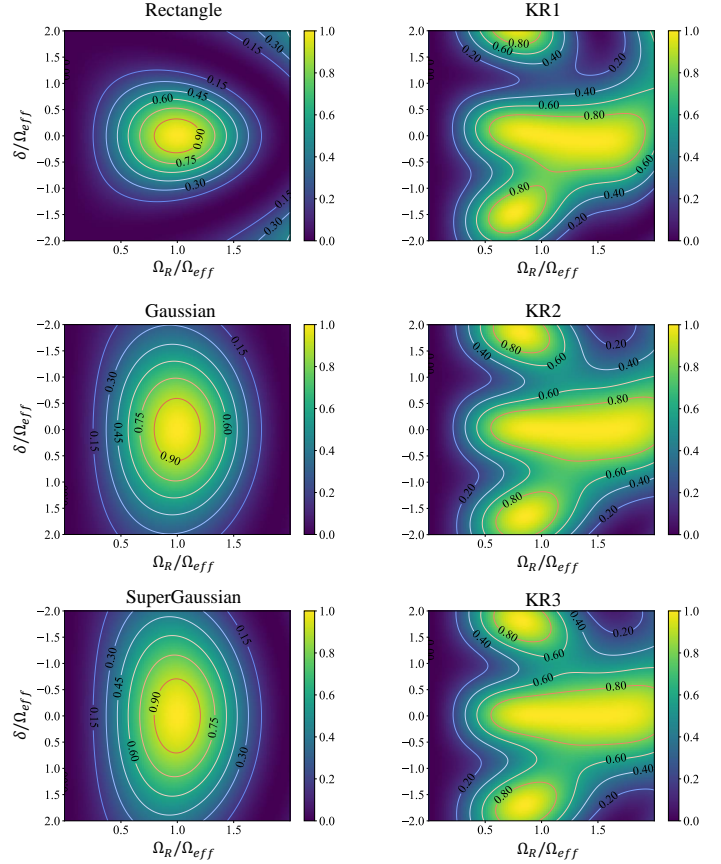


FIG. 6. Heat map comparison of the performance of different pulses in the two-dimensional error space of detuning and coupling strength. The right column shows the Krotov pulses optimized with three different step-size parameters λ (KR1, KR2, KR3); the left column shows three standard pulses (rectangular, Gaussian, and super-Gaussian) for comparison. In the plots, the horizontal axis is the normalized coupling strength, and the vertical axis is the detuning. The color and contour lines represent the atomic transition probability, with the bright yellow/red areas indicating high fidelity.

ence of a finite detuning (detuning = 0.2 times the Rabi frequency), as shown in Fig. 7.

From the comparison of trajectories in Fig. 7, it is clear that for the standard pulse in the presence of detuning, its effective rotation axis deviates from the Bloch sphere's equatorial plane. This causes the quantum state's evolution trajectory to be a tilted arc, and the final state fails to precisely reach the north pole from the south pole, resulting in a loss of fidelity. For the KR2 pulse, however, the trajectory is much more complex. It is no longer a simple in-plane rotation but instead traces out a carefully designed three-dimensional path on the surface of the sphere. By introducing specific phase and amplitude modulations during the evolution, this path actively compensates for the detrimental phase accumulation introduced by the detuning. This strategy of trading increased control complexity for insensitivity to error pa-

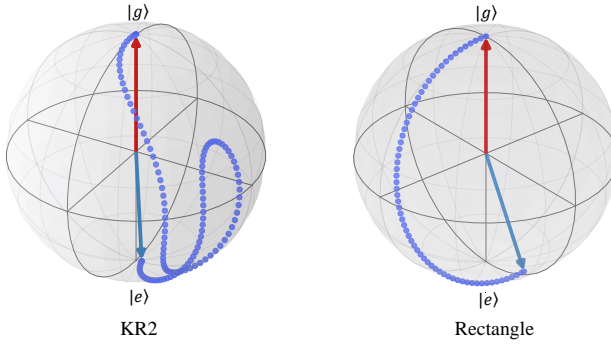


FIG. 7. Comparison of the quantum state evolution trajectories on the Bloch sphere in the presence of frequency detuning. The left panel shows the trajectory under the action of the optimized KR2 pulse. The right panel shows the trajectory under the action of a standard rectangular pulse. Both evolutions are simulated with a detuning equal to 0.2 times the Rabi frequency.

rameters is the core idea behind robust control schemes in modern quantum control, such as composite pulses and adiabatic pulses. The Krotov method automatically finds the optimal path to achieve this objective.

C. Gravimetry Performance

Ultimately, the performance of the Raman pulses must be tested by their practical application in an atom interferometer. In a Mach-Zehnder atom interferometer, the fidelity and robustness of the beam-splitter ($\pi/2$) and mirror (π) pulses directly determine the contrast of the final interference fringes. A higher contrast implies a stronger signal and a higher signal-to-noise ratio, which in turn enables more sensitive phase measurements.

To directly link the enhancement in pulse performance to the final measurement precision, we simulated the final interference fringes output by the atom interferometer when using our optimized KR2 pulse, a standard Gaussian pulse, and a standard rectangular pulse as the mirror π pulse, all under the condition of a fixed systematic error (a constant laser detuning). The results are shown in Fig. 8. The fringe contrast is defined as $C = P_{\max} - P_{\min}$, where P_{\max} and P_{\min} are the maximum and minimum atomic population probabilities of the fringe, respectively. By calculating the fringe contrast from the plots in Fig. 8, we find that for the standard pulses, the fringe amplitude is severely compressed and the contrast is significantly reduced due to their sensitivity to detuning. In contrast, when using the KR2 pulse, thanks to its excellent robustness, the resulting interference fringe has the largest oscillation amplitude, maintaining an extremely high contrast.

This result clearly demonstrates that the sensitivity of standard pulses to detuning (as shown in Fig. 5 and

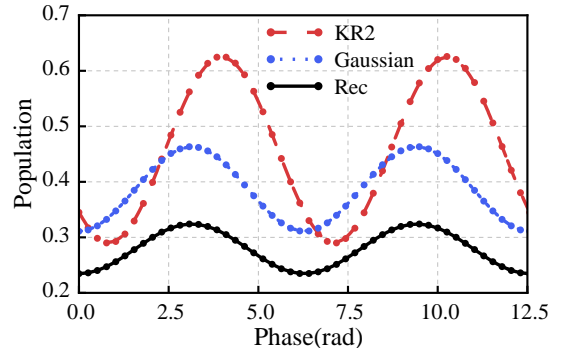


FIG. 8. Simulated final interference fringes for the atom interferometer using different mirror pulses under the condition of a fixed laser detuning. In the plot, the horizontal axis is the scanned phase of the interferometer, and the vertical axis is the final atomic population. The red curve (KR2) represents the case using the Krotov-optimized pulse, while the blue (Gaussian) and black (Rec) curves represent the cases using standard Gaussian and rectangular pulses, respectively.

Fig. 6) directly leads to a decrease in the coherence of the interferometric process, which ultimately manifests as a severe degradation of the fringe contrast. Conversely, the superior robustness of the KR2 pulse allows it to efficiently and precisely manipulate the atomic wave packet even in the presence of errors, thereby preserving the coherence of the interference signal to the greatest extent possible. The high fidelity and strong robustness obtained through the Krotov optimization method can effectively suppress the negative impact of realistic experimental noise on the interferometer's performance, ultimately translating into a significant enhancement of the interference signal's contrast. For applications such as precision gravimetry, this implies higher measurement sensitivity, precision, and long-term stability.

IV. CONCLUSION

To address the key issue of laser system noise limiting the performance of high-precision atom interferometers, this study has proposed and verified a scheme based on the Krotov quantum optimal control algorithm for designing highly robust Raman mirror pulses. Numerical simulations clearly show that, compared to standard pulses, the optimized pulses can maintain near-perfect atomic manipulation fidelity over a much broader range of noise parameters. More importantly, in the simulated interferometer, these pulses can effectively resist the influence of noise, which is directly linked to an enhancement in the signal-to-noise ratio and final precision of gravity measurements. This research confirms that quantum optimal control is an effective pathway for enhancing the performance of precision atomic sensors.

In future work, we plan to experimentally verify the op-

timized pulse scheme. We will also extend this optimization method to the $\pi/2$ beam-splitter pulses in the interferometer sequence and incorporate more comprehensive physical models, such as the atomic velocity distribution,

into the optimization process. The aim is to obtain globally optimal control solutions that more closely align with realistic experimental conditions.

[1] F. Flechtner, C. Reigber, R. Rummel, and G. Balmino, *Surveys in Geophysics* **42**, 1029–1074 (2021).

[2] T. E. Jensen, B. Dale, A. Stokholm, R. Forsberg, A. Bresson, N. Zahzam, A. Bonnin, and Y. Bidel, *Earth System Science Data* **17**, 1667–1684 (2025).

[3] G. Rosi, F. Sorrentino, L. Cacciapuoti, M. Prevedelli, and G. M. Tino, *Nature* **510**, 518–521 (2014).

[4] G. Lamporesi, A. Bertoldi, L. Cacciapuoti, M. Prevedelli, and G. M. Tino, *Physical Review Letters* **100**, 10.1103/physrevlett.100.050801 (2008).

[5] B. Canuel, F. Leduc, D. Holleville, A. Gauguet, J. Fils, A. Virdis, A. Clairon, N. Dimarcq, C. J. Bordé, A. Landragin, and P. Bouyer, *Physical Review Letters* **97**, 10.1103/physrevlett.97.010402 (2006).

[6] P. Cheiney, L. Fouché, S. Templier, F. Napolitano, B. Battelier, P. Bouyer, and B. Barrett, *Physical Review Applied* **10**, 10.1103/physrevapplied.10.034030 (2018).

[7] S. M. Dickerson, J. M. Hogan, A. Sugarbaker, D. M. S. Johnson, and M. A. Kasevich, *Physical Review Letters* **111**, 10.1103/physrevlett.111.083001 (2013).

[8] M. Kasevich and S. Chu, *Physical Review Letters* **67**, 181–184 (1991).

[9] C. R. Ekstrom, J. Schmiedmayer, M. S. Chapman, T. D. Hammond, and D. E. Pritchard, *Physical Review A* **51**, 3883–3888 (1995).

[10] R. Bouchendira, P. Cladé, S. Guellati-Khélifa, F. Nez, and F. Biraben, *Physical Review Letters* **106**, 10.1103/physrevlett.106.080801 (2011).

[11] A. Bonnin, N. Zahzam, Y. Bidel, and A. Bresson, *Physical Review A* **92**, 10.1103/physreva.92.023626 (2015).

[12] P. Asenbaum, C. Overstreet, M. Kim, J. Curti, and M. A. Kasevich, *Physical Review Letters* **125**, 10.1103/physrevlett.125.191101 (2020).

[13] X. Wu, Z. Pagel, B. S. Malek, T. H. Nguyen, F. Zi, D. S. Scheirer, and H. Müller, *Science Advances* **5**, 10.1126/sciadv.aax0800 (2019).

[14] S. S. Szigeti, J. E. Debs, J. J. Hope, N. P. Robins, and J. D. Close, *New Journal of Physics* **14**, 023009 (2012).

[15] J. Le Gouët, T. Mehlstäubler, J. Kim, S. Merlet, A. Clairon, A. Landragin, and F. Pereira Dos Santos, *Applied Physics B* **92**, 133–144 (2008).

[16] G. Jäger, D. M. Reich, M. H. Goerz, C. P. Koch, and U. Hohenester, *Physical Review A* **90**, 10.1103/physreva.90.033628 (2014).

[17] D. Daems, A. Ruschhaupt, D. Sugny, and S. Guérin, *Physical Review Letters* **111**, 10.1103/physrevlett.111.050404 (2013).

[18] S. van Frank, A. Negretti, T. Berrada, R. Bücker, S. Montangero, J.-F. Schaff, T. Schumm, T. Calarco, and J. Schmiedmayer, *Nature Communications* **5**, 10.1038/ncomms5009 (2014).

[19] D. M. Reich, M. Ndong, and C. P. Koch, *The Journal of Chemical Physics* **136**, 10.1063/1.3691827 (2012).

[20] S. J. Glaser, U. Boscain, T. Calarco, C. P. Koch, W. Köckenberger, R. Kosloff, I. Kuprov, B. Luy, S. Schirmer, T. Schulte-Herbrüggen, D. Sugny, and F. K. Wilhelm, *The European Physical Journal D* **69**, 10.1140/epjd/e2015-60464-1 (2015).

[21] J. C. Saywell, M. S. Carey, P. S. Light, S. S. Szigeti, A. R. Milne, K. S. Gill, M. L. Goh, V. S. Perunicic, N. M. Wilson, C. D. Macrae, A. Rischka, P. J. Everitt, N. P. Robins, R. P. Anderson, M. R. Hush, and M. J. Biercuk, *Nature Communications* **14**, 10.1038/s41467-023-43374-0 (2023).

[22] B. W. Shore, *Manipulating Quantum Structures Using Laser Pulses* (Cambridge University Press, 2011).

[23] P. R. Berman, *Atom Interferometry* (Cambridge University Press, 1997).

[24] J. C. Saywell, I. Kuprov, D. Goodwin, M. Carey, and T. Freegarde, *Physical Review A* **98**, 10.1103/physreva.98.023625 (2018).

[25] A. Dunning, R. Gregory, J. Bateman, N. Cooper, M. Himsorth, J. A. Jones, and T. Freegarde, *Physical Review A* **90**, 10.1103/physreva.90.033608 (2014).

[26] C. López-Monjaraz, H. Peña Vega, K. Jiménez-García, J. M. López Romero, and N. V. Corzo, *Physica Scripta* **99**, 125414 (2024).

[27] W. Magnus, *Communications on Pure and Applied Mathematics* **7**, 649–673 (1954).

[28] X. Miao, *Physics Letters A* **271**, 296–302 (2000).

[29] Y. Luo, S. Yan, Q. Hu, A. Jia, C. Wei, and J. Yang, *The European Physical Journal D* **70**, 10.1140/epjd/e2016-70428-6 (2016).

[30] T. M. Brzozowski, M. Maczynska, M. Zawada, J. Zaczorowski, and W. Gawlik, *Journal of Optics B: Quantum and Semiclassical Optics* **4**, 62–66 (2002).

[31] R. Stoner, D. Butts, J. Kinast, and B. Timmons, *Journal of the Optical Society of America B* **28**, 2418 (2011).

[32] D. L. Butts, J. M. Kinast, B. P. Timmons, and R. E. Stoner, *Journal of the Optical Society of America B* **28**, 416 (2011).

[33] Y. Wang, J. Cheng, Y. Liu, and T. Lin, *Physical Review A* **109**, 10.1103/physreva.109.053501 (2024).

[34] V. F. Krotov and H. Kong (1993).

[35] O. Morzhin and A. Pechen (arXiv, 2018).

[36] J. Saywell, M. Carey, M. Belal, I. Kuprov, and T. Freegarde, *Journal of Physics B: Atomic, Molecular and Optical Physics* **53**, 085006 (2020).

[37] J. P. Palao and R. Kosloff, *Physical Review A* **68**, 10.1103/physreva.68.062308 (2003).

[38] J. P. Palao, R. Kosloff, and C. P. Koch, *Physical Review A* **77**, 10.1103/physreva.77.063412 (2008).

[39] I. Serban, J. Werschnik, and E. K. U. Gross, *Physical Review A* **71**, 10.1103/physreva.71.053810 (2005).

[40] A. Kaiser and V. May, *The Journal of Chemical Physics* **121**, 2528–2535 (2004).

[41] S. E. Sklarz and D. J. Tannor, *Physical Review A* **66**, 10.1103/physreva.66.053619 (2002).

[42] K. Kobzar, T. E. Skinner, N. Khaneja, S. J. Glaser, and B. Luy, *Journal of Magnetic Resonance* **194**, 58–66

(2008).
[43] K. Kobzar, T. E. Skinner, N. Khaneja, S. J. Glaser, and B. Luy, *Journal of Magnetic Resonance* **170**, 236–243 (2004).